

# NeRF-Guided Unsupervised Learning of RGB-D Registration

Zhinan Yu<sup>1\*</sup>, Zheng Qin<sup>2\*</sup>, Yijie Tang<sup>1</sup>, Yongjun Wang<sup>1</sup>, Renjiao Yi<sup>1</sup>,  
Chenyang Zhu<sup>1</sup>, and Kai Xu<sup>1†</sup>

<sup>1</sup> National University of Defense Technology, China

<sup>2</sup> Defense Innovation Institute, Academy of Military Sciences, China

**Abstract.** This paper focuses on training a robust RGB-D registration model without ground-truth pose supervision. Existing methods usually adopt a pairwise training strategy based on differentiable rendering, which enforces the photometric and the geometric consistency between the two registered frames as supervision. However, this frame-to-frame framework suffers from poor multi-view consistency due to factors such as lighting changes, geometry occlusion and reflective materials. In this paper, we present NeRF-UR, a novel frame-to-model optimization framework for unsupervised RGB-D registration. Instead of frame-to-frame consistency, we leverage the neural radiance field (NeRF) as a global model of the scene and use the consistency between the input and the NeRF-rerendered frames for pose optimization. This design can significantly improve the robustness in scenarios with poor multi-view consistency and provides better learning signal for the registration model. Furthermore, to bootstrap the NeRF optimization, we create a synthetic dataset, Sim-RGBD, through a photo-realistic simulator to warm up the registration model. By first training the registration model on Sim-RGBD and later unsupervisedly fine-tuning on real data, our framework enables distilling the capability of feature extraction and registration from simulation to reality. Our method outperforms the state-of-the-art counterparts on two popular indoor RGB-D datasets, ScanNet and 3DMatch. Code and models will be released for paper reproduction.

**Keywords:** RGB-D registration · unsupervised learning · NeRF

## 1 Introduction

The difficulty of 3D data acquisition has significantly diminished owing to the substantial increase in RGB-D sensor availability and a concurrent decrease in costs. The prolific collection of RGB-D data has greatly propelled the advancement of deep learning in the field of 3D vision, resulting in substantial improvements in the performance of applications such as RGB-D SLAM and RGB-D

---

\*Equal contribution.

†Corresponding author.

reconstruction. A pivotal challenge in achieving reliable 3D reconstruction based on discrete RGB-D image frames lies in establishing correct inter-frame associations, through means such as feature matching, to facilitate camera pose estimation. Motivated by these, our goal is to devise a robust registration model for RGB-D images, thereby providing robust and high-quality pixel-level matching for RGB-D registration.

Traditional methods, relying on hand-crafted features (such as SIFT [21]) find difficulty in handling complex and noisy real-world data. Deep learning based methods, on the other hand, have gained much attention lately and most works adopt a supervised learning approach [1, 27, 41, 42] to accomplish robust registration. These learning-based methods can support RGB-D registration between frames even with very small overlaps. The performance of supervised learning approaches, however, depends highly on the quality of the data annotation, i.e., ground-truth frame poses, which are difficult to obtain and hence limit their application in practice.

To overcome the reliance on annotated data in learning-based methods, the exploration of better strategies to extract information from unlabeled data for achieving unsupervised learning in RGB-D registration has gradually become a research focus. Inspired by works in multi-view geometry, studies have found that the geometric and photometric consistency inherent in the RGB-D sequences of a scene can offer effective supervision for feature extraction. To our knowledge, UR&R [12] is the first work proposing an unsupervised framework for RGB-D point cloud registration. It takes two RGB-D frames with overlap as input and estimates their relative pose with a registration model [37, 43]. Based on this relative pose, UR&R rerenders one frame to the reference frame of the other with a point cloud-based differentiable rasterization mechanism, and enforces the photometric and geometric consistency between the rerendered and the input frames to enable training of the registration model. However, this frame-to-frame optimization lacks global contextual information of the entire scene, especially in cases with limited distinctive features, making it vulnerable to scenarios with poor multi-view consistency due to factors such as lighting and occlusion (see Fig. 1). Furthermore, point cloud-based methods require large overlap to enable high-quality rerendering which limits its applicability in more challenging cases.

We introduce **NeRF-guided Unsupervised Registration (NeRF-UR)**, an unsupervised RGB-D registration framework based on frame-to-model optimization. To overcome the limitations of frame-to-frame optimization, we adopt the neural radiance fields (NeRF) as the global model to support unsupervised training. Note, however, that the initialization of the NeRF requires accurate frame poses but we cannot achieve this without a good registration model, which makes a *chicken-and-egg* problem. So we opt to utilize synthetic RGB-D data rendered with 3D scene models to train an initial registration model to bootstrap the frame-to-model optimization. To this end, we create a synthetic dataset, Sim-RGBD, with photo-realistic rendering of CAD models, which contains more than 100k rendered images of 90 scenes. As shown in Fig 1, the registration model is first trained on Sim-RGBD with the ground-truth poses and later unsupervisedly

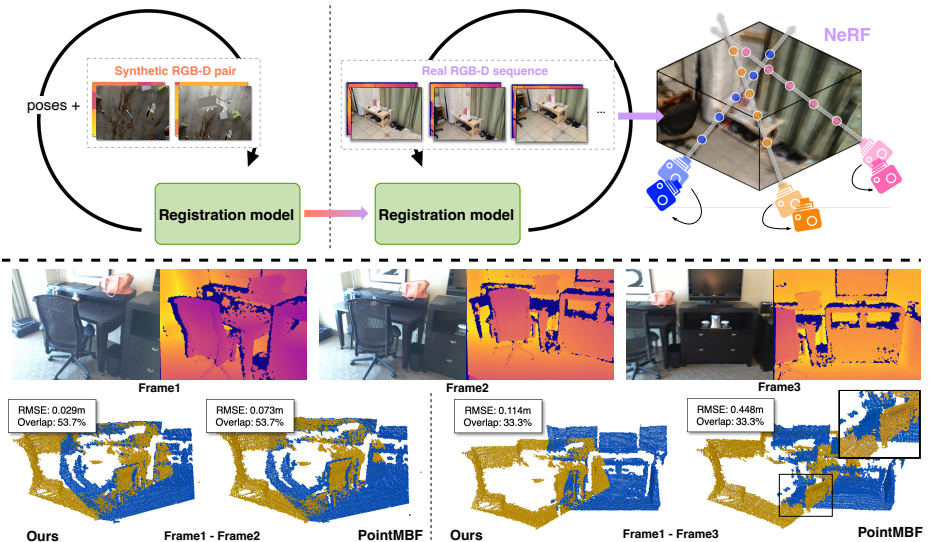


**Fig. 1:** We propose NeRF-UR, a frame-to-model optimization framework for unsupervised RGB-D registration. The registration is first bootstrapped with synthetic data, and then fine-tuned on real-world data under guidance of NeRF (top). Although the frame-to-frame method can successfully register the easy case (bottom-left), it cannot register the case with lighting changes and low overlap (bottom-right). On the contrary, our method effectively register the hard case.

fine-tuned on the real-world data in a frame-to-model manner. As the NeRF is constructed from the entire RGB-D sequence, it can better handle multi-view inconsistency factors such as lighting changes, geometry occlusion and reflective materials. Therefore, enforcing the photometric and geometric consistency between the NeRF re-rendering and the input frames can better optimize the estimated poses than the frame-to-frame methods, which enhances the learning signal for the registration model.

This refining stage enables distilling the capability of feature extraction and registration from simulation to real world.

We have evaluated our method on two popular indoor RGB-D datasets, ScanNet [7] and 3DMatch [44]. We demonstrate that our method outperforms both traditional and recent unsupervised learning-based registration pipelines. Moreover, our method achieves significantly better performance than previous methods in more challenging scenarios with lower overlap or severe lighting changes.

Extensive ablation studies are conducted to prove the effectiveness of different components of our pipeline. In summary, our contributions are as follows:

- We propose a NeRF-guided frame-to-model optimization framework for unsupervised RGB-D registration. The infusion of global reconstruction information enhances the reliability of re-rendering errors, which fortifies the robustness of our registration model.

- We devise a synthetic bootstrap mechanism to provide high-quality initial poses for NeRF optimization and create a synthetic dataset for warming up RGB-D registration model.
- Our method achieves new state-of-the-art results on the two popular indoor RGB-D datasets, ScanNet and 3DMatch.

## 2 Related Work

### 2.1 Point Cloud Registration

Point cloud registration is a problem of estimating the transformation matrix between two frames of scanned point clouds. The key lies in how to detect features with specificity from the two-frame point cloud, how to construct accurate correlations, and how to utilize accurate rigid transformations extracted from these correspondences. Since deep learning has been found good at feature representation, how to learn robust and invariant visual features through deep learning networks has become a focus of research. [11, 24–27, 36] Many Feature learning methods [1, 2, 5, 6, 8, 16, 27, 37, 40, 42] were proposed. They get the point cloud features by neural network and use a robust estimator e.g. RANSAC to estimate the final rigid transformation. Different from focusing on feature learning, there are some end-to-end learning-based registration methods [14, 19, 22, 35, 39] that treat the registration as a regression problem. They encoded the transformations into the implicit space as a parameter in the network optimization process.

### 2.2 Unsupervised Point Cloud Registration

The aforementioned methods rely on ground-truth poses to supervised the training. The ground-truth pose is often obtained by reconstruction of the SfM, which suffers from high computational overhead and instability. Recently, unsupervised RGB-D registration methods have been proposed to bypass the need of pose annotations. To our knowledge, UR&R [12] is the first unsupervised registration framework by introducing a differentiable render-based loss to optimize the feature extractor. BYOC [13] stands for the fact that randomly initialized CNNs also provide relatively good correspondences, proposed a teacher-student framework to train their feature extractor. LLT [37] fused the geometric and visual information in a more trivial way by introducing a multi-scale local linear transformation to fuse RGB and depth modalities. PointMBF [43] has designed a network based on unidirectional fusion to better extract and fuse features from geometric and visual sources and has achieved state-of-the-art performance. However, these methods have difficulty in handling multi-view inconsistency caused by factors such as lighting changes, highlight or occlusion. In this work, we design a NeRF-guided frame-to-model framework to address this issue.

## 2.3 Pose Optimization in Neural SLAM

Existing Neural SLAM methods [20, 30, 32, 34, 38, 45, 46] incorporate neural implicit representations into RGB-D SLAM systems, allowing tracking and mapping from scratch. The groundbreaking work, iMAP [30], encode both the color and geometry of the scene into a MLP. This MLP can be jointly optimized with a batch of poses through rendering loss. In the subsequent works, NICE-SLAM [46] and Vox-Fusion [38] introduce a hybrid representation that combines learnable grid-based features with a neural decoder, enabling the utilization of local scene color and geometry to guide pose optimization. More recently, Mips-fusion [32] proposed a robust and scalable RGB-D reconstruction system with a multi-implicit-submap neural representation. Co-SLAM [34] proposed a joint coordinate and sparse-parametric encoding and a more global bundle adjustment approach. Inspired by the aforementioned works, we introduce our framework for estimating the initial camera pose using a feature extractor and subsequently refining the pose through implicit 3D reconstruction.

## 3 Method

### 3.1 Overview

Given two RGB-D frames  $\mathcal{X} = (\mathbf{I}^{\mathcal{X}}, \mathbf{X})$  and  $\mathcal{Y} = (\mathbf{I}^{\mathcal{Y}}, \mathbf{Y})$ , where  $\mathbf{I}^{\mathcal{X}}, \mathbf{I}^{\mathcal{Y}} \in \mathbb{R}^{H \times W \times 3}$  are the RGB images and  $\mathbf{X} \in \mathbb{R}^{N^{\mathcal{X}} \times 3}$ ,  $\mathbf{Y} \in \mathbb{R}^{N^{\mathcal{Y}} \times 3}$  are the point clouds backprojected from the corresponding depth images, our goal is to recover the 6-DoF relative pose  $\mathbf{T} \in \mathcal{SE}(3)$  between them, which consists of a 3D rotation  $\mathbf{R} \in \mathcal{SO}(3)$  and a 3D translation  $\mathbf{t} \in \mathbb{R}^3$ . To solve this problem, recent deep registration methods first extract point features  $\mathbf{F}^{\mathcal{X}} \in \mathbb{R}^{N^{\mathcal{X}} \times C}$  and  $\mathbf{F}^{\mathcal{Y}} \in \mathbb{R}^{N^{\mathcal{Y}} \times C}$  for the two frames with a point cloud registration model  $\mathcal{F}$ :

$$\mathbf{F}^{\mathcal{X}} = \mathcal{F}(\mathbf{I}^{\mathcal{X}}, \mathbf{X}), \quad \mathbf{F}^{\mathcal{Y}} = \mathcal{F}(\mathbf{I}^{\mathcal{Y}}, \mathbf{Y}), \quad (1)$$

and then extract point correspondences  $\mathcal{C} = \{(\mathbf{p}_i, \mathbf{q}_i) \mid \mathbf{p}_i \in \mathbf{X}, \mathbf{q}_i \in \mathbf{Y}\}$  via feature matching. The relative pose is then estimated based on the correspondences. Obviously, the discriminativeness of the extracted features accounts for the quality of the resultant relative pose. However, the training of  $\mathcal{F}$  heavily relies on the ground-truth pose  $\mathbf{T}^* = \{\mathbf{R}^*, \mathbf{t}^*\}$ , which suffers from great annotation difficulty and unstable convergence.

In this work, we propose an unsupervised point cloud registration method named *NeRF-UR*. Our method leverages unposed RGB-D sequences to train the registration model  $\mathcal{F}$ . To achieve effective supervision, we generate high-quality relative pose in a NeRF-guided manner (Sec. 3.3). To bootstrap the parameters of  $\mathcal{F}$ , we build a scene-level synthetic dataset and pretrain  $\mathcal{F}$  on this dataset so that reasonable initial features can be learned (Sec. 3.4). Fig. 2 illustrates the overall pipeline of our method.

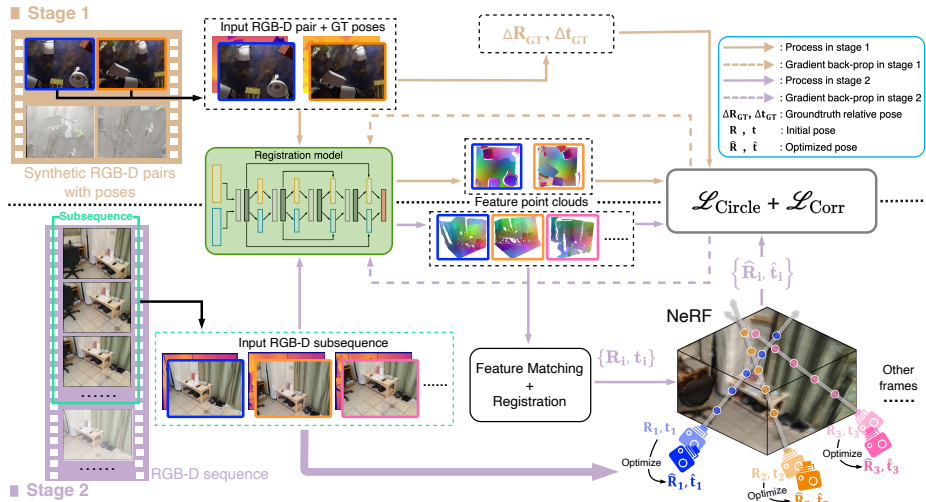


**Fig. 2:** Overall pipeline of NeRF-UR. Our framework can be divided into two stages. The first synthetic bootstrap stage leverages synthetic RGB-D pairs as well as their ground-truth poses to train the registration model in a supervised manner. In the second frame-to-model optimization stage, we take an RGB-D sequence as input and use the registration model to estimate the relative pose for every two consecutive frames. Based on the estimated poses, we jointly optimize a NeRF model of the whole scene and the estimated poses. At last, the optimized poses are used to fine-tune the registration model on real-world data.

## 3.2 Registration Model

We use PointMBF [43] as our registration model, which fuses the information from both the visual (2D) and the geometric (3D) spaces for better feature distinctiveness. Our model contains two branches, *i.e.*, the visual branch and the geometric branch. The visual branch is a modified ResNet-18 [17] network, following a U-shape architecture. The geometric branch is a KPFCN [2, 33] network symmetric with the visual branch. Both branches adopt a three-stage architecture, and a PointNet-based fusion module fuses the features from the two modalities after each stage. Moreover, we would note that, although an RGB-D model is used here, our method is encoder-agnostic and can also work with only the visual branch [12] or the geometric branch [6].

## 3.3 NeRF-Guided Unsupervised Registration

An unsupervised registration pipeline relies on high-quality poses to supervise the registration model. However, unsupervised registration is more prone to outliers, which significantly harm the quality of relative poses. Existing methods [12, 37, 43] use differentiable rasterization and optimize the frame pose according to the photometric and the geometric consistency between two nearby

frames from an RGB-D sequence. Nevertheless, the consistency between two frames are easily to be affected by occlusion or lighting changes under different viewpoints, which fails to effectively refine the frame poses and thus harms the training of the registration model. This has inspired us that a more comprehensive modeling of the whole scene is required to effectively optimize the frame poses. Recently, NeRF [23] has the ability to model the lighting and geometric structures in a scene, and jointly optimize 3D maps and poses [34, 46]. Based on this insight, we propose to train the registration model scene by scene and optimize a NeRF for each scene for pose refinement. By leveraging the NeRF, we optimize the poses in a *frame-to-model* fashion instead of the traditional frame-to-frame one, which can better handle the occlusion and lighting changes.

**Pipeline.** As shown in Fig. 2, to avoid the error accumulation and the huge time overhead caused by joint map-pose optimization in large scenes, we opt to process small subscenes instead of the whole scene. Specifically, we split the RGB-D sequence of a scene into subsequences of 200 frames, and we optimize a NeRF for each subsequence. Within each subsequence, we further sample keyframes every 20 frames for training and all other frames are omitted. The reference frame of the first keyframe is treated as the global reference frame of the subscene. For each keyframe, we first register it with the previous keyframe with  $\mathcal{F}$  to obtain its initial pose, and then insert it into the NeRF to jointly optimize its pose and the map. At last, we use the optimized pose of each keyframe to supervise the registration model.

**Initial pose generation.** Given two keyframes, we first extract their point features  $\mathbf{F}^{\mathcal{X}}$  and  $\mathbf{F}^{\mathcal{Y}}$  with  $\mathcal{F}$ , which are  $\ell_2$ -normalized onto a unit sphere. For each point  $\mathbf{x}_i \in \mathbf{X}$ , we then find its nearest point  $\mathbf{y}_{n_i} \in \mathbf{Y}$  in the feature space as a correspondence. The weight for each correspondence is computed as:

$$w_i = 1 - \frac{\|\mathbf{f}_i^{\mathcal{X}} - \mathbf{f}_{n_i}^{\mathcal{Y}}\|}{2}. \quad (2)$$

At last, we select the top  $k$  correspondences with the largest weights. The same computation goes for  $\mathbf{Y}$ . As a result, we obtain  $2k$  correspondences, denoted as  $\mathcal{C}$ . To compute the initial pose, we randomly sample 10 correspondence subsets of 20% of the correspondences. For each subset, we use weighted SVD [3] to compute a pose hypothesis and select the best pose which minimizes:

$$E = \sum_{(\mathbf{p}_i, \mathbf{q}_i) \in \mathcal{C}} w_i \|\mathbf{R}\mathbf{p}_i + \mathbf{t} - \mathbf{q}_i\|. \quad (3)$$

**Pose optimization.** We adopt a NeRF model similar with Co-SLAM [34] due to its advances in the speed and the quality of reconstruction. Our NeRF maps the world coordinates  $\mathbf{x} = (x, y, z)$  and the viewing direction  $\mathbf{d} = (\theta, \phi)$  into the color  $\mathbf{c}$  and the TSDF value  $s$ . Following the SLAM pipeline, for each keyframe, our method can be split into the *Tracking* stage and *Mapping* stage.

In the tracking stage, we optimize the pose of the keyframe with the NeRF. The optimized pose in this stage is named the *tracked pose*, denoted as  $\tilde{\mathbf{T}}_i$ . For

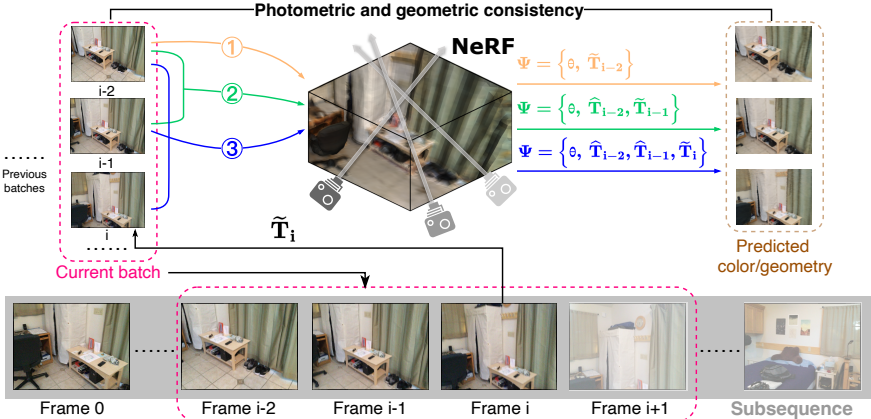


**Fig. 3:** Mapping stage. Once the  $i$ -th frame is tracked, it will be added to the current batch along with its tracked pose  $\tilde{\mathbf{T}}_i$ . The optimizable parameters for each round comprise the scene parameter vector  $\theta$  and the poses of frames present in the current batch, encompassing both tracked poses  $\tilde{\mathbf{T}}$ , which have recently been incorporated, and optimized poses  $\hat{\mathbf{T}}$  from previous rounds. The colored arrows (orange, green, and blue) depict the optimization process in different rounds, while  $\Psi$  denotes the set of optimizable parameters.

the  $i$ -th keyframe, we first calculate its untracked pose  $\mathbf{T}_i = \Delta\mathbf{T}_{i-1,i} \cdot \hat{\mathbf{T}}_{i-1}$ , where  $\hat{\mathbf{T}}_{i-1}$  is the mapped pose of the previous keyframe as described later and  $\Delta\mathbf{T}_{i-1,i}$  is their initial relative pose from the registration model.  $\mathbf{T}_i$  is then optimized to  $\tilde{\mathbf{T}}_i$  by supervising the photometric and the geometric consistency between the input RGB-D frame and the re-rendered frame by the NeRF. The NeRF parameters are fixed in this stage. Please refer to the supplementary material for more details about the NeRF training. As the NeRF implicitly models the whole scene, this frame-to-model paradigm could alleviate the influence of heavy occlusion or lighting changes from different viewpoints, and thus achieves more effective optimization of the keyframe pose.

After one keyframe is tracked, we jointly optimize the NeRF parameters and the poses of the keyframes in the mapping stage. The pose refined in this stage is named the *mapped pose*, denoted as  $\mathbf{T}_i$ . The mapping stage adopts a batch-wise optimization strategy. When a keyframe is tracked, it is added into the current batch. Then all keyframes in this batch are used to optimize the NeRF parameters to improve the implicit scene model, with their poses being optimized simultaneously. This joint optimization further improves the quality of the keyframe poses. After we have collected a maximal batch size  $B$  of keyframes, we train the registration model with the mapped poses of the keyframes in the current batch. The batch is then emptied except the last keyframe, which is used to provides the anchor pose for the coming keyframes in the next batch.

**Training the registration model.** After obtaining the optimized poses of a batch, we compute the relative poses between consecutive keyframes which are used as the frame poses to train the registration model. We first compute correspondences between two keyframes with their optimized poses and then apply the circle loss [18, 31] and the correspondence loss (Eq. 3) during training. Please refer to the supplementary material for more details.

### 3.4 Synthetic Bootstrap

Jointly optimizing the NeRF parameters and the poses of keyframes requires relatively accurate initial poses. However, a randomly initialized registration model tends to generate enormous outlier correspondences. This causes the initial poses to be erroneous, and thus leads to suboptimal convergence. To address this issue, we propose to leverage synthetic data to bootstrap the registration model. With the synthetic data, we can warm up the registration model in supervision by the ground-truth poses so that it can provide reasonable initial poses.

**Sim-RGBD dataset.** To bootstrap the model training, we first construct a synthetic dataset using photo-realistic simulation with BlenderProc [9], named *Sim-RGBD*. Sim-RGBD consists of 90 scenes, which are split into 60 training scenes and 30 validation scenes. Specifically, for each scene, we create two boxes centered at  $(0, 0, 0)$  in the sizes of respectively  $10\text{m} \times 10\text{m} \times 5\text{m}$  and  $6\text{m} \times 6\text{m} \times 3\text{m}$ , and uniformly select 400 positions in the space between them. We then place a random object model from ShapeNet dataset [4] at each position, which is randomly rotated, translated, and scaled.

After constructing the synthetic scenes, we render 400 pairs of RGB-D frames from each scene. Another problem here is how to sample appropriate camera poses to ensure the synthetic pairs are more realistic. To this end, we opt to first sample the pose of the source frame, and then sample the relative pose between the source and the target frames. For the source pose, the camera direction is determined by a random pitch angle between  $[15^\circ, 75^\circ]$  and a random yaw angle between  $[0^\circ, 360^\circ]$ . And the camera position is determined by a random distance between  $[0.7\text{m}, 1.5\text{m}]$  from  $(0, 0, 0)$  along this direction. For the relative pose, we first randomly sample a rotation axis, and then sample the rotation angle from  $\mathcal{N}(20^\circ, 15^\circ)$  and the translation from  $\mathcal{N}(0.4\text{m}, 0.2\text{m})$ .

As the two rendered frames could have little overlap, we only preserve the pairs with the overlap ratio above 0.3. As shown in Sec 4.3, the synthetic scenes simulated with this simplistic strategy effectively bootstrap the model.

**Training settings.** Similar to Sec. 3.3, we use the ground-truth poses to retrieve correspondences and apply the circle loss to train the registration model. Note that it is important to ensure the bootstrapping stage and the NeRF-guided learning stage to use the same training strategy. Otherwise, the two models could be in different feature spaces, thus harming the final performance.

## 4 Experiments

We conduct our experiments on three RGB-D datasets, 3DMatch [44], ScanNet [7], and Sim-RGBD, which is constructed using photo-realistic simulation for pre-training. The experimental content is outlined as follows. Initially, we introduce experimental design in Sec. 4.1. Next, we introduce experimental outcomes in Sec. 4.2 and show the superiority of our method by giving the corresponding experimental data. Subsequently, we also conduct sufficient ablation experiments in Sec. 4.3 on our method, aiming to analyze the specific contributions of each module within our overall design. The qualitative results are shown in Sec. 4.4.

### 4.1 Experimental Settings

**Datasets.** We conduct extensive experiments on two large real-world datasets 3DMatch [44] and ScanNet [7], together with a synthetic dataset Sim-RGBD. All of them contain RGB-D images, camera intrinsic, and ground-truth camera poses. For the ScanNet dataset [7], we follow its original training/testing/validation split and divide it into three parts, which contain 1045/312/100 scenes for each. Then we randomly select 300 scenes for training in the train split. For the 3DMatch dataset [44], we follow its original training/testing/validation split and divide it into three parts, which contain 71/19/11 scenes for each. For the Sim-RGBD dataset, we split it into 62/28 scenes for training/testing.

**Implementation Details.** We adopted some settings from PointMBF [43], such as data processing, learning rate, and so on. On the software side, our code is built using PyTorch [28] and PyTorch3D [28]. And on the hardware side, our network is training with an Nvidia GeForce RTX 3090Ti GPU with 24GB memory and an Intel<sup>®</sup> Core<sup>™</sup> i9-12900K @ 3.9GHz  $\times$  16 with 32GB RAM.

**Metrics.** We follow previous work [12, 37, 43] and use rotation error, translation error, and chamfer error as our evaluation metrics. Each metric is reported with three different thresholds with a mean and median value. In addition, we follow settings in [12, 37, 43] to generate view pairs by sampling images pairs which are 20 frames apart. Also we evaluate view pairs by sampling frames with 50 frames apart. However, as the test data lacks overlap in certain segments of the 50 frame apart, its evaluation markedly distorts both the mean and median values. Consequently, we opt not to include these results in our experiment presentation.

**Baseline Methods.** We compare our method with baselines from three categories, (1) traditional methods: ICP [3], FPFH [29] SIFT [21], (2) learning-based supervised methods: SuperPoint [10], FCGF [6], DGR [5], 3D MV Reg [15] and REGTR [40], and (3) unsupervised methods: UR&R [12], BYOC [13], LLT [37] and PointMBF [43]. We use the results of the baselines reported by [37, 43].

**Table 1: Pairwise registration on ScanNet [7] dataset with a 20 frames apart.** Sup means supervision.

| Train Set        | Sup     | Rotation( $^{\circ}$ ) |             |                    |             |            | Translation(cm)     |             |                    |             |            | Chamfer(mm)         |             |                    |             |            |            |
|------------------|---------|------------------------|-------------|--------------------|-------------|------------|---------------------|-------------|--------------------|-------------|------------|---------------------|-------------|--------------------|-------------|------------|------------|
|                  |         | Accuracy $\uparrow$    |             | Error $\downarrow$ |             |            | Accuracy $\uparrow$ |             | Error $\downarrow$ |             |            | Accuracy $\uparrow$ |             | Error $\downarrow$ |             |            |            |
|                  |         | 5                      | 10          | 45                 | Mean        | Med.       | 5                   | 10          | 25                 | Mean        | Med.       | 1                   | 5           | 10                 | Mean        | Med.       |            |
| ICP [3]          | -       | 31.7                   | 55.6        | 99.6               | 10.4        | 8.8        | 7.5                 | 19.4        | 74.6               | 22.4        | 20.0       | 8.4                 | 24.7        | 40.5               | 32.9        | 14.1       |            |
| FPFH [29]        | -       | 34.1                   | 64.0        | 90.3               | 20.6        | 7.2        | 8.8                 | 26.7        | 66.8               | 42.6        | 18.6       | 27.0                | 60.8        | 73.3               | 23.3        | 2.9        |            |
| SIFT [21]        | -       | 55.2                   | 75.7        | 89.2               | 18.6        | 4.3        | 17.7                | 44.5        | 79.8               | 26.5        | 11.2       | 38.1                | 70.6        | 78.3               | 42.6        | 1.7        |            |
| SuperPoint [10]  | -       | 65.5                   | 86.9        | 96.6               | 8.9         | 3.6        | 21.2                | 51.7        | 88.0               | 16.1        | 9.7        | 45.7                | 81.1        | 88.2               | 19.2        | 1.2        |            |
| FCGF [6]         | -       | $\checkmark$           | 70.2        | 87.7               | 96.2        | 9.5        | 3.3                 | 27.5        | 58.3               | 82.9        | 23.6       | 8.3                 | 52.0        | 78.0               | 83.7        | 24.4       | 0.9        |
| DGR [5]          | 3DMatch | $\checkmark$           | 81.1        | 89.3               | 94.8        | 9.4        | 1.8                 | 54.5        | 76.2               | 88.7        | 18.4       | 4.5                 | 70.5        | 85.5               | 89.0        | 13.7       | 0.4        |
| 3D MV Reg [15]   | 3DMatch | $\checkmark$           | 87.7        | 93.2               | 97.0        | 6.0        | 1.2                 | 69.0        | 83.1               | 91.8        | 11.7       | 2.9                 | 78.9        | 89.2               | 91.8        | 10.2       | 0.2        |
| REGTR [40]       | 3DMatch | $\checkmark$           | 86.0        | 93.9               | 98.6        | 4.4        | 1.6                 | 61.4        | 80.3               | 91.4        | 14.4       | 3.8                 | 80.9        | 90.9               | 93.6        | 13.5       | 0.2        |
| UR&R [12]        | 3DMatch |                        | 87.6        | 93.1               | 98.3        | 4.3        | 1.0                 | 69.2        | 84.0               | 93.8        | 9.5        | 2.8                 | 79.7        | 91.3               | 94.0        | 7.2        | 0.2        |
| UR&R(RGB-D)      | 3DMatch |                        | 87.6        | 93.7               | 98.8        | 3.8        | 1.1                 | 67.5        | 83.8               | 94.6        | 8.5        | 3.0                 | 78.6        | 91.7               | 94.6        | 6.5        | 0.2        |
| UR&R(Supervised) | 3DMatch | $\checkmark$           | 92.3        | 95.3               | 98.2        | 3.8        | <b>0.8</b>          | 77.6        | 89.4               | 95.5        | 7.8        | 2.3                 | 86.1        | 94.0               | 95.6        | 6.7        | <b>0.1</b> |
| BYOC [13]        | 3DMatch |                        | 66.5        | 85.2               | 97.8        | 7.4        | 3.3                 | 30.7        | 57.6               | 88.9        | 16.0       | 8.2                 | 54.1        | 82.8               | 89.5        | 9.5        | 0.9        |
| LLT [37]         | 3DMatch |                        | 93.4        | 96.5               | 98.8        | 2.5        | <b>0.8</b>          | 76.9        | 90.2               | 96.7        | 5.5        | 2.2                 | 86.4        | 95.1               | 95.8        | 4.6        | <b>0.1</b> |
| PointMBF [43]    | 3DMatch |                        | 94.6        | 97.0               | 98.7        | 3.0        | <b>0.8</b>          | 81.0        | 92.0               | 97.1        | 6.2        | <b>2.1</b>          | 91.3        | 96.6               | 97.4        | 4.9        | <b>0.1</b> |
| Ours             | 3DMatch |                        | <b>97.2</b> | <b>99.0</b>        | <b>99.7</b> | <b>1.6</b> | 0.9                 | <b>84.2</b> | <b>95.8</b>        | <b>98.7</b> | <b>3.9</b> | 2.2                 | <b>93.2</b> | <b>98.3</b>        | <b>98.8</b> | <b>2.7</b> | <b>0.1</b> |
| UR&R [12]        | ScanNet |                        | 92.7        | 95.8               | 98.5        | 3.4        | 0.8                 | 77.2        | 89.6               | 96.1        | 7.3        | 2.3                 | 86.0        | 94.6               | 96.1        | 5.9        | <b>0.1</b> |
| UR&R(RGB-D)      | ScanNet |                        | 94.1        | 97.0               | 99.1        | 2.6        | 0.8                 | 78.4        | 91.1               | 97.3        | 5.9        | 2.3                 | 87.3        | 95.6               | 97.2        | 5.0        | <b>0.1</b> |
| BYOC [13]        | ScanNet |                        | 86.5        | 95.2               | 99.1        | 3.8        | 1.7                 | 56.4        | 80.6               | 96.3        | 8.7        | 4.3                 | 78.1        | 93.9               | 96.4        | 5.6        | 0.3        |
| LLT [37]         | ScanNet |                        | 95.5        | 97.6               | 99.1        | 2.5        | 0.8                 | 80.4        | 92.2               | 97.6        | 5.5        | 2.2                 | 88.9        | 96.4               | 97.6        | 4.6        | <b>0.1</b> |
| PointMBF [43]    | ScanNet |                        | 96.0        | 97.6               | 98.9        | 2.5        | <b>0.7</b>          | 83.9        | 93.8               | 97.7        | 5.6        | <b>1.9</b>          | 92.8        | 97.3               | 97.9        | 4.7        | <b>0.1</b> |
| Ours             | ScanNet |                        | <b>97.8</b> | <b>99.2</b>        | <b>99.8</b> | <b>1.4</b> | 0.8                 | <b>86.9</b> | <b>96.3</b>        | <b>98.9</b> | <b>3.6</b> | 2.0                 | <b>94.3</b> | <b>98.5</b>        | <b>99.0</b> | <b>2.6</b> | <b>0.1</b> |

## 4.2 Quantitative Results

We claim our experimental comparison with existing methods in Table. 1 and Table. 2. Our framework is bootstrapped on the Sim-RGBD dataset and fine-tuned on ScanNet [7] and 3DMatch [44], respectively. In Table. 1, we primarily present the results on the ScanNet test scene with 20 frames apart. Due to this 20 frames apart, the overlap in the images is limited, posing challenges in demonstrating the superiority of our method. Therefore, in Table. 2, we present the results of our method alongside PointMBF on the ScanNet test scene with 50 frames apart. The experimental results show the superiority of our method.

**Evaluate on 20 frames apart.** Our approach achieved considerable improvement and outperformed the competitors. It is worth noting that, compared to the current state-of-the-art method pointMBF, we make more progress in training on the 3DMatch dataset. As in the Table. 1, we gain a 2.6 percentage point in the rotation accuracy in the threshold of  $5^{\circ}$ , 3.2 percentage point in the translation accuracy in the threshold of 5 cm, 1.9 percentage point in the Chamfer distance accuracy in the threshold of 1 mm, respectively. The result shows that the registration model obtained by training our method has better generalization. Also, the results of training on ScanNet prove our superiority. Above, we find that the NeRF-Guided unsupervised strategy is of great significance. Our two-stage NeRF-guided training approach is designed to more effectively harness the capabilities of the registration model, resulting in improved performance.

**Table 2: Pairwise registration on ScanNet with a 50 frames apart setting.**

|           |         | Rotation( $^{\circ}$ ) |             |             | Translation(cm)     |             |             | Chamfer(mm)         |             |             |
|-----------|---------|------------------------|-------------|-------------|---------------------|-------------|-------------|---------------------|-------------|-------------|
| Train Set |         | Accuracy $\uparrow$    |             |             | Accuracy $\uparrow$ |             |             | Accuracy $\uparrow$ |             |             |
|           |         | 5                      | 10          | 45          | 5                   | 10          | 25          | 1                   | 5           | 10          |
| PointMBF  | 3DMatch | 59.3                   | 62.5        | 76.6        | 34.2                | 47.9        | 61.6        | 42.9                | 55.8        | 60.2        |
| Ours      | 3DMatch | <b>76.4</b>            | <b>84.8</b> | <b>92.6</b> | <b>46.9</b>         | <b>69.4</b> | <b>81.9</b> | <b>60.3</b>         | <b>77.7</b> | <b>80.8</b> |
| PointMBF  | ScanNet | 60.4                   | 68.2        | 79.9        | 40.0                | 54.3        | 66.9        | 48.9                | 61.5        | 65.8        |
| Ours      | ScanNet | <b>78.8</b>            | <b>85.9</b> | <b>93.0</b> | <b>51.0</b>         | <b>72.7</b> | <b>83.6</b> | <b>63.9</b>         | <b>79.9</b> | <b>82.6</b> |

**Table 3: Ablation on rendering strategy.** Rasterization denotes the rasterization process, which renders RGB and depth images from the aligned point cloud. Neural denotes that we optimize the input global pose by neural rendering in NeRF and use this optimized pose to supervise the registration model.

|               |         | Rotation( $^{\circ}$ ) |             |             | Translation(cm)     |             |             | Chamfer(mm)         |             |             |
|---------------|---------|------------------------|-------------|-------------|---------------------|-------------|-------------|---------------------|-------------|-------------|
| Train Set     |         | Accuracy $\uparrow$    |             |             | Accuracy $\uparrow$ |             |             | Accuracy $\uparrow$ |             |             |
|               |         | 5                      | 10          | 45          | 5                   | 10          | 25          | 1                   | 5           | 10          |
| Rasterization | ScanNet | 73.6                   | 80.4        | 87.5        | 48.6                | 67.4        | 78.3        | 59.9                | 74.7        | 77.7        |
| Neural        | ScanNet | <b>78.8</b>            | <b>85.9</b> | <b>93.0</b> | <b>51.0</b>         | <b>72.7</b> | <b>83.6</b> | <b>63.9</b>         | <b>79.9</b> | <b>82.6</b> |

**Evaluate on 50 frames apart.** Since the test with a 20 frame apart is not enough to show the capability of our method with a large overlap, we separately compared our method with the current state-of-the-art method with a 50 frame apart setting in Table. 2. It is evident that our method achieves higher accuracy even with a smaller overlap.

### 4.3 Ablation Study

To verify the role of the various parts in our pipeline, we design multiple ablation studies. We conducted related experiments on real datasets as well. In the following experiments, our model underwent a bootstrapping operation on the synthetic dataset Sim-RGBD, unless otherwise specified.

**Comparison with other rendering strategies.** In our pipeline, the point cloud rasterization step in recent unsupervised RGB-D point cloud registration methods is replaced with the construction of NeRF to achieve unsupervised training. We believe that constructing NeRF using multi-frame RGB-D images, as opposed to their approach of using only two frames for point cloud rasterization, can better leverage photometric and geometric consistency in the scene. This, in turn, provides more effective supervisory signals for the registration model.

The results in Table. 3 indicate that, under the same settings, i.e., when our registration model undergoes the same bootstrap process on a synthetic dataset, the NeRF-guided approach outperforms their point cloud rasterization

**Table 4: Ablation on bootstrap module.** Bootstrap denotes the process of training the registration model on the Sim-RGBD dataset.

| Bootstrap | Train Set | Rotation( $^{\circ}$ ) |             |             | Translation(cm)     |             |             | Chamfer(mm)         |             |             |
|-----------|-----------|------------------------|-------------|-------------|---------------------|-------------|-------------|---------------------|-------------|-------------|
|           |           | Accuracy $\uparrow$    |             |             | Accuracy $\uparrow$ |             |             | Accuracy $\uparrow$ |             |             |
|           |           | 5                      | 10          | 45          | 5                   | 10          | 25          | 1                   | 5           | 10          |
|           | 3DMatch   | 65.2                   | 76.8        | 90.4        | 35.0                | 58.4        | 74.2        | 49.0                | 68.4        | 72.8        |
| ✓         | 3DMatch   | <b>76.4</b>            | <b>84.8</b> | <b>92.6</b> | <b>46.9</b>         | <b>69.4</b> | <b>81.9</b> | <b>60.3</b>         | <b>77.7</b> | <b>80.8</b> |
|           | ScanNet   | 73.0                   | 82.9        | 92.3        | 44.2                | 66.6        | 80.2        | 57.3                | 75.2        | 79.2        |
| ✓         | ScanNet   | <b>78.8</b>            | <b>85.9</b> | <b>93.0</b> | <b>51.0</b>         | <b>72.7</b> | <b>83.6</b> | <b>63.9</b>         | <b>79.9</b> | <b>82.6</b> |

**Table 5: Ablation on fine-tuning module.** FT denotes fine-tuning registration model after bootstrapping on the train set.  $N_t$  denotes the number of iterators for tracking. Blanks in the  $N_t$  indicate that no fine-tuning operation was performed.

| FT | $N_t$ | Train Set | Rotation( $^{\circ}$ ) |             |             | Translation(cm)     |             |             | Chamfer(mm)         |             |             |
|----|-------|-----------|------------------------|-------------|-------------|---------------------|-------------|-------------|---------------------|-------------|-------------|
|    |       |           | Accuracy $\uparrow$    |             |             | Accuracy $\uparrow$ |             |             | Accuracy $\uparrow$ |             |             |
|    |       |           | 5                      | 10          | 45          | 5                   | 10          | 25          | 1                   | 5           | 10          |
|    |       | ScanNet   | 74.4                   | 81.3        | 89.5        | 49.6                | 68.5        | 79.0        | 61.0                | 75.6        | 78.3        |
| ✓  |       | ScanNet   | 76.6                   | 85.2        | <b>93.5</b> | 46.6                | 70.0        | 82.9        | 60.1                | 78.7        | 82.0        |
| ✓  | 20    | ScanNet   | 77.6                   | 85.5        | 93.2        | 48.4                | 70.8        | 82.7        | 61.6                | 78.9        | 82.1        |
| ✓  | 100   | ScanNet   | <b>78.8</b>            | <b>85.9</b> | 93.0        | <b>51.0</b>         | <b>72.7</b> | <b>83.6</b> | <b>63.9</b>         | <b>79.9</b> | <b>82.6</b> |

method. This finding further validates the correctness and effectiveness of the NeRF-Guided framework proposed in this study.

**Effect of bootstrap module.** In the preceding discussion, it is mentioned that the construction of NeRF requires a relatively accurate initial camera pose. We have observed that performing bootstrapping on a synthetic dataset can assist the registration model in providing a better camera pose when operating in real-world scenes. We consider the bootstrapping process to be essential, as the absence of this stage significantly degrades the final performance. Consequently, we conduct an ablation study on the presence or absence of bootstrapping.

The results are shown in Table. 4. Our findings indicate a substantial decrease in performance when the bootstrapping operation is omitted. This aligns with our hypothesis that without a sufficiently good initial camera pose, the effectiveness of NeRF in camera pose optimization diminishes, and in some cases, may even result in no improvement at all.

**Effect of fine-tuning module.** To demonstrate the necessity of using NeRF for pose optimization, we conduct this ablation study. We test four models on the ScanNet dataset, each representing a different training strategy: a registration model obtained after bootstrapping, a registration model fine-tuned using the pose generated by RANSAC, a registration model fine-tuned using the pose

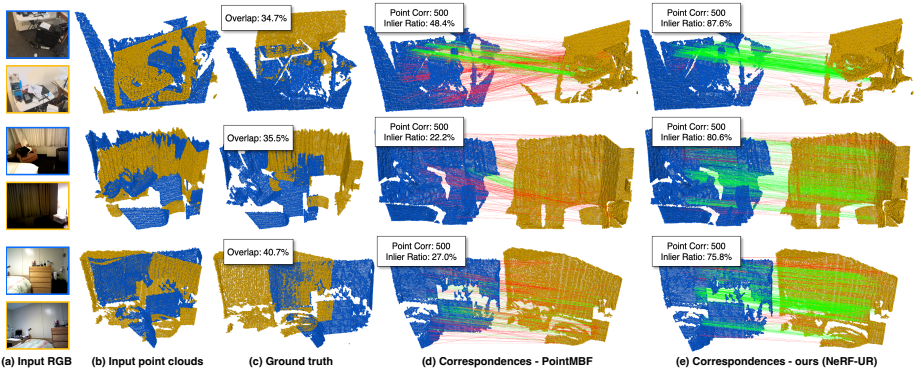


**Fig. 4: Correspondences results with PointMBF and NeRF-UR.** The first row indicates that NeRF-UR performs better when input point clouds have a low overlap ratio. The following rows demonstrate that even under drastic lighting changes, where other methods are significantly affected, our method can still perform well.

optimized by NeRF with 20 iterations for tracking, and a registration model fine-tuned using the pose optimized by NeRF with 100 iterations for tracking.

The results are shown in Table. 5. Based on the results of this ablation study, we made two key findings. First, the fine-tuning operation on real-world scenes is crucial. Second, the quality of the pose, used to generate supervisory signals, plays a critical role in the model’s performance.

#### 4.4 Qualitative Results

Fig. 4 provides a gallery of the correspondence results of the model trained on ScanNet with PointMBF and NeRF-UR. The NeRF-Guided unsupervised registration enables the registration model to perform better on scenes with smaller overlaps (1<sup>st</sup> row) and more dramatic changes in lighting conditions (2<sup>nd</sup> and 3<sup>rd</sup> rows) between relative frames.

## 5 Conclusion

We have presented NeRF-UR, a frame-to-model optimization framework for unsupervised RGB-D registration. Our method constructs a NeRF and enforces the photometric and the geometric consistency between the input and the NeRF-rendered frames to optimize the estimated poses from the registration model. This design can effectively improve the robustness to lighting changes, geometry occlusion and reflective materials. We further devise a bootstrap mechanism on synthetic dataset to warm up the NeRF optimization. Extensive experiments on two benchmarks have demonstrated the efficiency of our method. We think the NeRF-guided unsupervised learning is a promising mechanism for 3D vision and we would like to extend it to more tasks such as localization, reconstruction, etc in the future.

## References

1. Ao, S., Hu, Q., Yang, B., Markham, A., Guo, Y.: Spinnet: Learning a general surface descriptor for 3d point cloud registration. In: Proceedings of the IEEE/CVF conference on computer vision and pattern recognition. pp. 11753–11762 (2021) [2](#), [4](#)
2. Bai, X., Luo, Z., Zhou, L., Fu, H., Quan, L., Tai, C.L.: D3feat: Joint learning of dense detection and description of 3d local features. In: Proceedings of the IEEE/CVF conference on computer vision and pattern recognition. pp. 6359–6367 (2020) [4](#), [6](#)
3. Besl, P.J., McKay, N.D.: Method for registration of 3-d shapes. In: Sensor fusion IV: control paradigms and data structures. vol. 1611, pp. 586–606. Spie (1992) [7](#), [10](#), [11](#)
4. Chang, A.X., Funkhouser, T., Guibas, L., Hanrahan, P., Huang, Q., Li, Z., Savarese, S., Savva, M., Song, S., Su, H., et al.: Shapenet: An information-rich 3d model repository. arXiv preprint arXiv:1512.03012 (2015) [9](#)
5. Choy, C., Dong, W., Koltun, V.: Deep global registration. In: Proceedings of the IEEE/CVF conference on computer vision and pattern recognition. pp. 2514–2523 (2020) [4](#), [10](#), [11](#)
6. Choy, C., Park, J., Koltun, V.: Fully convolutional geometric features. In: Proceedings of the IEEE/CVF international conference on computer vision. pp. 8958–8966 (2019) [4](#), [6](#), [10](#), [11](#)
7. Dai, A., Chang, A.X., Savva, M., Halber, M., Funkhouser, T., Nießner, M.: Scannet: Richly-annotated 3d reconstructions of indoor scenes. In: Proceedings of the IEEE conference on computer vision and pattern recognition. pp. 5828–5839 (2017) [3](#), [10](#), [11](#)
8. Deng, H., Birdal, T., Ilic, S.: Ppfnet: Global context aware local features for robust 3d point matching. In: Proceedings of the IEEE conference on computer vision and pattern recognition. pp. 195–205 (2018) [4](#)
9. Denninger, M., Winkelbauer, D., Sundermeyer, M., Boerdijk, W., Knauer, M.W., Strobl, K.H., Humt, M., Triebel, R.: Blenderproc2: A procedural pipeline for photorealistic rendering. *Journal of Open Source Software* **8**(82), 4901 (2023) [9](#)
10. DeTone, D., Malisiewicz, T., Rabinovich, A.: Superpoint: Self-supervised interest point detection and description. In: Proceedings of the IEEE conference on computer vision and pattern recognition workshops. pp. 224–236 (2018) [10](#), [11](#)
11. Duan, Y., Zhu, C., Lan, Y., Yi, R., Liu, X., Xu, K.: Disarm: displacement aware relation module for 3d detection. In: Proceedings of the IEEE/CVF Conference on Computer Vision and Pattern Recognition. pp. 16980–16989 (2022) [4](#)
12. El Banani, M., Gao, L., Johnson, J.: Unsuperviseddr&r: Unsupervised point cloud registration via differentiable rendering. In: Proceedings of the IEEE/CVF Conference on Computer Vision and Pattern Recognition. pp. 7129–7139 (2021) [2](#), [4](#), [6](#), [10](#), [11](#)
13. El Banani, M., Johnson, J.: Bootstrap your own correspondences. In: Proceedings of the IEEE/CVF International Conference on Computer Vision. pp. 6433–6442 (2021) [4](#), [10](#), [11](#)
14. Elbaz, G., Avraham, T., Fischer, A.: 3d point cloud registration for localization using a deep neural network auto-encoder. In: Proceedings of the IEEE conference on computer vision and pattern recognition. pp. 4631–4640 (2017) [4](#)
15. Gojcic, Z., Zhou, C., Wegner, J.D., Guibas, L.J., Birdal, T.: Learning multiview 3d point cloud registration. In: Proceedings of the IEEE/CVF conference on computer vision and pattern recognition. pp. 1759–1769 (2020) [10](#), [11](#)

16. Gojcic, Z., Zhou, C., Wegner, J.D., Wieser, A.: The perfect match: 3d point cloud matching with smoothed densities. In: Proceedings of the IEEE/CVF conference on computer vision and pattern recognition. pp. 5545–5554 (2019) [4](#)
17. He, K., Zhang, X., Ren, S., Sun, J.: Deep residual learning for image recognition. In: Proceedings of the IEEE conference on computer vision and pattern recognition. pp. 770–778 (2016) [6](#)
18. Huang, S., Gojcic, Z., Usvyatsov, M., Wieser, A., Schindler, K.: Predator: Registration of 3d point clouds with low overlap. In: Proceedings of the IEEE/CVF Conference on computer vision and pattern recognition. pp. 4267–4276 (2021) [9](#)
19. Huang, X., Mei, G., Zhang, J.: Feature-metric registration: A fast semi-supervised approach for robust point cloud registration without correspondences. In: Proceedings of the IEEE/CVF conference on computer vision and pattern recognition. pp. 11366–11374 (2020) [4](#)
20. Johari, M.M., Carta, C., Fleuret, F.: Eslam: Efficient dense slam system based on hybrid representation of signed distance fields. In: Proceedings of the IEEE/CVF Conference on Computer Vision and Pattern Recognition. pp. 17408–17419 (2023) [5](#)
21. Lowe, D.G.: Distinctive image features from scale-invariant keypoints. *International journal of computer vision* **60**, 91–110 (2004) [2](#), [10](#), [11](#)
22. Lu, W., Wan, G., Zhou, Y., Fu, X., Yuan, P., Song, S.: Deepvcp: An end-to-end deep neural network for point cloud registration. In: Proceedings of the IEEE/CVF international conference on computer vision. pp. 12–21 (2019) [4](#)
23. Mildenhall, B., Srinivasan, P.P., Tancik, M., Barron, J.T., Ramamoorthi, R., Ng, R.: Nerf: Representing scenes as neural radiance fields for view synthesis. *Communications of the ACM* **65**(1), 99–106 (2021) [7](#)
24. Pan, L., Chen, X., Cai, Z., Zhang, J., Zhao, H., Yi, S., Liu, Z.: Variational relational point completion network. In: Proceedings of the IEEE/CVF conference on computer vision and pattern recognition. pp. 8524–8533 (2021) [4](#)
25. Qi, C.R., Su, H., Mo, K., Guibas, L.J.: Pointnet: Deep learning on point sets for 3d classification and segmentation. In: Proceedings of the IEEE conference on computer vision and pattern recognition. pp. 652–660 (2017) [4](#)
26. Qi, C.R., Yi, L., Su, H., Guibas, L.J.: Pointnet++: Deep hierarchical feature learning on point sets in a metric space. *Advances in neural information processing systems* **30** (2017) [4](#)
27. Qin, Z., Yu, H., Wang, C., Guo, Y., Peng, Y., Xu, K.: Geometric transformer for fast and robust point cloud registration. In: Proceedings of the IEEE/CVF conference on computer vision and pattern recognition. pp. 11143–11152 (2022) [2](#), [4](#)
28. Ravi, N., Reizenstein, J., Novotny, D., Gordon, T., Lo, W.Y., Johnson, J., Gkioxari, G.: Accelerating 3d deep learning with pytorch3d. arXiv:2007.08501 (2020) [10](#)
29. Rusu, R.B., Blodow, N., Beetz, M.: Fast point feature histograms (fpfh) for 3d registration. In: 2009 IEEE international conference on robotics and automation. pp. 3212–3217. IEEE (2009) [10](#), [11](#)
30. Sucar, E., Liu, S., Ortiz, J., Davison, A.J.: imap: Implicit mapping and positioning in real-time. In: Proceedings of the IEEE/CVF International Conference on Computer Vision. pp. 6229–6238 (2021) [5](#)
31. Sun, Y., Cheng, C., Zhang, Y., Zhang, C., Zheng, L., Wang, Z., Wei, Y.: Circle loss: A unified perspective of pair similarity optimization. In: Proceedings of the IEEE/CVF conference on computer vision and pattern recognition. pp. 6398–6407 (2020) [9](#)

32. Tang, Y., Zhang, J., Yu, Z., Wang, H., Xu, K.: Mips-fusion: Multi-implicit-submaps for scalable and robust online neural rgb-d reconstruction. *ACM Transactions on Graphics (TOG)* **42**(6), 1–16 (2023) [5](#)
33. Thomas, H., Qi, C.R., Deschaud, J.E., Marcotegui, B., Goulette, F., Guibas, L.J.: Kpconv: Flexible and deformable convolution for point clouds. In: *Proceedings of the IEEE/CVF international conference on computer vision*. pp. 6411–6420 (2019) [6](#)
34. Wang, H., Wang, J., Agapito, L.: Co-slam: Joint coordinate and sparse parametric encodings for neural real-time slam. In: *Proceedings of the IEEE/CVF Conference on Computer Vision and Pattern Recognition*. pp. 13293–13302 (2023) [5](#), [7](#)
35. Wang, L., Chen, J., Li, X., Fang, Y.: Non-rigid point set registration networks. *arXiv preprint arXiv:1904.01428* (2019) [4](#)
36. Wang, X., Xu, Y., Xu, K., Tagliasacchi, A., Zhou, B., Mahdavi-Amiri, A., Zhang, H.: Pie-net: Parametric inference of point cloud edges. *Advances in neural information processing systems* **33**, 20167–20178 (2020) [4](#)
37. Wang, Z., Huo, X., Chen, Z., Zhang, J., Sheng, L., Xu, D.: Improving rgb-d point cloud registration by learning multi-scale local linear transformation. In: *European Conference on Computer Vision*. pp. 175–191. Springer (2022) [2](#), [4](#), [6](#), [10](#), [11](#)
38. Yang, X., Li, H., Zhai, H., Ming, Y., Liu, Y., Zhang, G.: Vox-fusion: Dense tracking and mapping with voxel-based neural implicit representation. In: *2022 IEEE International Symposium on Mixed and Augmented Reality (ISMAR)*. pp. 499–507. IEEE (2022) [5](#)
39. Yang, Z., Pan, J.Z., Luo, L., Zhou, X., Grauman, K., Huang, Q.: Extreme relative pose estimation for rgb-d scans via scene completion. In: *Proceedings of the IEEE/CVF Conference on Computer Vision and Pattern Recognition*. pp. 4531–4540 (2019) [4](#)
40. Yew, Z.J., Lee, G.H.: Regtr: End-to-end point cloud correspondences with transformers. In: *Proceedings of the IEEE/CVF conference on computer vision and pattern recognition*. pp. 6677–6686 (2022) [4](#), [10](#), [11](#)
41. Yu, H., Li, F., Saleh, M., Busam, B., Ilic, S.: Cofinet: Reliable coarse-to-fine correspondences for robust pointcloud registration. *Advances in Neural Information Processing Systems* **34**, 23872–23884 (2021) [2](#)
42. Yu, H., Qin, Z., Hou, J., Saleh, M., Li, D., Busam, B., Ilic, S.: Rotation-invariant transformer for point cloud matching. In: *Proceedings of the IEEE/CVF Conference on Computer Vision and Pattern Recognition*. pp. 5384–5393 (2023) [2](#), [4](#)
43. Yuan, M., Fu, K., Li, Z., Meng, Y., Wang, M.: Pointmbf: A multi-scale bidirectional fusion network for unsupervised rgb-d point cloud registration. In: *Proceedings of the IEEE/CVF International Conference on Computer Vision*. pp. 17694–17705 (2023) [2](#), [4](#), [6](#), [10](#), [11](#)
44. Zeng, A., Song, S., Nießner, M., Fisher, M., Xiao, J., Funkhouser, T.: 3dmatch: Learning local geometric descriptors from rgb-d reconstructions. In: *Proceedings of the IEEE conference on computer vision and pattern recognition*. pp. 1802–1811 (2017) [3](#), [10](#), [11](#)
45. Zhang, Y., Tosi, F., Mattocchia, S., Poggi, M.: Go-slam: Global optimization for consistent 3d instant reconstruction. In: *Proceedings of the IEEE/CVF International Conference on Computer Vision*. pp. 3727–3737 (2023) [5](#)
46. Zhu, Z., Peng, S., Larsson, V., Xu, W., Bao, H., Cui, Z., Oswald, M.R., Pollefeys, M.: Nice-slam: Neural implicit scalable encoding for slam. In: *Proceedings of the IEEE/CVF Conference on Computer Vision and Pattern Recognition*. pp. 12786–12796 (2022) [5](#), [7](#)